

Unsupervised and Unregistered Hyperspectral Image Super-Resolution with Mutual Dirichlet-Net

Ying Qu, *Member, IEEE*, Hairong Qi, *Fellow, IEEE* and Chiman Kwan *Senior Member, IEEE*,

Abstract—Hyperspectral images (HSI) provide rich spectral information that has contributed to the successful performance improvement of numerous computer vision tasks. However, it can only be achieved at the expense of images' spatial resolution. Hyperspectral image super-resolution (HSI-SR) thus addresses this problem by fusing low resolution (LR) HSI with multispectral image (MSI) carrying much higher spatial resolution (HR). All existing HSI-SR approaches require the LR HSI and HR MSI to be well registered and the reconstruction accuracy of the HR HSI relies heavily on the registration accuracy of different modalities. This paper exploits the uncharted problem domain of HSI-SR *without the requirement of multi-modality registration*. The success of this endeavor would largely facilitate the deployment of HSI-SR since registration requirement is difficult to satisfy in real-world sensing devices. Given the unregistered LR HSI and HR MSI with overlapped regions, we design a unique unsupervised learning structure linking the two unregistered modalities by projecting them into the same statistical space through the same encoder. The mutual information (MI) is further adopted to capture the non-linear statistical dependencies between the representations from two modalities (carrying spatial information) and their raw inputs. By maximizing the MI, spatial correlations between different modalities can be well characterized to further reduce the spectral distortion. We assume the representations follow a similar Dirichlet distribution pattern for its inherent sum-to-one and non-negative properties. A collaborative $l_{2,1}$ norm is employed as the reconstruction error instead of the more common l_2 norm, so that individual pixels can be recovered as accurately as possible. With this design, the network allows to extract correlated spectral and spatial information from unregistered images that better preserves the spectral information. The proposed method is referred to as unregistered and unsupervised mutual Dirichlet Net (u^2 -MDN). Extensive experimental results using benchmark HSI datasets demonstrate the superior performance of u^2 -MDN as compared to the state-of-the-art.

Index Terms—Hyperspectral image, super-resolution, unregistered, mutual information, deep learning, unsupervised, Dirichlet-Net

I. INTRODUCTION

Hyperspectral image (HSI) collects hundreds of contiguous spectral representations of objects, which demonstrates advantages over conventional multispectral image (MSI) or RGB image with much less spectral information [1], [2]. Compared to conventional images, the rich spectral information of HSI can effectively distinguish visually similar objects that actually consist of different materials. Thus, HSI has been shown to

Ying Qu, and Hairong Qi are with the Advanced Imaging and Collaborative Information Processing Group, Department of Electrical Engineering and Computer Science, University of Tennessee, Knoxville, TN 37996 USA (e-mail: yqu3@vols.utk.edu; hqi@utk.edu).

Chiman Kwan is with Applied Research LLC, Rockville, MD, 20850 USA (chiman.kwan@arllc.net)

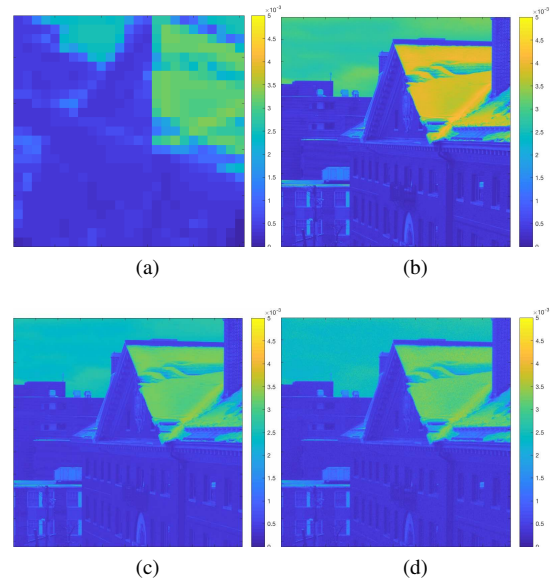


Fig. 1. Unregistered hyperspectral image super-resolution. (a) First band of the 20 degree rotated and cropped LR HSI with 38% information missing. (b) First band of the HR MSI. (c) First band of the reconstructed HR HSI by the proposed methods. (d) First band of the reference HR HSI.

enhance the performance of a wide range of computer vision tasks, such as, object recognition and classification [3]–[9], segmentation [10], tracking [11]–[14], environmental monitoring [15], [16], and change detection [17]–[19].

During the HSI acquisition process, the finer the spectral resolution, the smaller the radiation energy that can reach the sensor for a particular spectral band within narrow wavelength range. Thus, the high spectral resolution of HSI can only be achieved at the cost of its spatial resolution due to the hardware limitations [20], [21]. On the contrary, we can obtain conventional MSI or RGB with much higher spatial resolution by integrating the radiation energy over broad spectral bands which inevitably reduces their spectral resolution significantly [22]. To improve the spatial resolution of HSI for better application performance, a natural way is to fuse the high spectral information extracted from HSI with the high-resolution spatial information extracted from conventional images to yield high resolution images in both spatial and spectral domains [8], [23], [24]. This procedure is referred to as *hyperspectral image super-resolution (HSI-SR)* [21], [22], [25].

The problem of HSI-SR originates from multispectral image super-resolution (MSI-SR) in remote sensing field, which has

been intensively studied over the past several decades [26]–[29]. Traditional HSI-SR methods extended from MSI-SR mainly include component substitution (CS) [26], [27], [29] and multi-resolution analysis (MRA) based methods [28]. However, they suffer from spectral distortion. Existing approaches specifically designed for HSI-SR can be broadly divided into two categories, *i.e.*, matrix factorization based and Bayesian based approaches [8], [30], [31]. Matrix factorization based methods [20], [22], [31]–[33] generally assume that the LR HSI is down-sampled from the HR HSI, and such a down-sampling function is adopted as a prior in the fusion procedure. In practice, the down-sampling function may not exist due to the complex environmental conditions. Bayesian based approaches reconstruct the HR HSI by extracting spectral information from LR HSI and spatial information from HR MSI separately [21], [34], [35]. However, the spectral information extracted from LR HSI may not be the optimal spectral bases for MSI, since MSI is not utilized at all during the optimization procedure. So in summary, spectral distortion can be easily introduced during the optimization procedure of methods from both categories.

HSI-SR is also closely related to natural image super-resolution, which usually trains a mapping function between synthetic LR images and its corresponding HR images [36]–[50], [50], [51] on large high resolution image dataset, in a supervised fashion. There have been several attempts to address the MSI-SR or HSI-SR problem with supervised deep learning where the mapping function is learned using different frameworks [43], [52]–[56]. However, these deep learning based methods, are all supervised, making their adoption on HSI-SR a challenge due to three reasons. First, the scale differences between LR HSI and HR MSI can reach as large as 10, *i.e.*, one pixel in HSI covers 100 pixels in MSI. In some applications, the scale difference can even be 25 [57] and 30 [58]. But most existing super resolution methods only work on up to 8 times upscaling. Second, they are designed to find an end-to-end mapping function between the LR images and HR images under the assumption that the mapping function is the same for different images. However, the mapping function may not be the same for images acquired with different sensors. Even for the data collected from the same sensor, the mapping function for different spectral bands may not be the same. Thus the assumption may cause severe spectral distortion. Third, training a mapping function is a supervised problem which requires a large dataset, the down-sampling function, and the availability of the HR HSI, making supervised learning unrealistic for HSI.

Despite a plethora of works on HSI-SR, all current approaches require at least one pre-requisite to solve the problem of HSI-SR, *i.e.*, the two input modalities (HSI and MSI) must be well registered, and the quality of the reconstructed HR HSI relies heavily on the registration accuracy [2], [8], [19], [24], [59]. According to previous works, there are a few methods that introduce registration as a pre-step before data fusion [30], [60], [61]. However, these pre-steps can only handle small scale differences, *e.g.*, two pixels/eight pixels offset in LR HSI/HR MSI [59]. Moreover, even in the registration community, HSI and MSI registration is a

challenging problem itself as one pixel in LR HSI may cover hundreds of pixels in the corresponding HR MSI. And the spectral difference is also large that both spectral response function (SRF) and multi-band images have to be taken into consideration during registration [59], [62]–[65]. Thus, most registration approaches can only handle small scale differences.

In this paper, an unsupervised network structure is proposed, aiming to solve the HSI-SR problem directly without multi-modality registration. An example is shown in Fig. 1. We address the problem based on the assumption that, the pixels in the overlapped region of HR HSI and HR MSI can be approximated by a linear combination of the same spectral information (spectral bases) with the same corresponding spatial information (representations), which indicates how the spectral basis are constructed for each pixel. Since LR HSI are the down-sampled version of the HR HSI, ideally, its representations should be correlated with that of the HR MSI and HR HSI, *i.e.*, they should follow similar patterns and distributions although possessing different resolutions, as shown in Fig. 2. Therefore, to reconstruct HR HSI with minimum spectral distortion, the network is designed to decouple both the LR HSI and HR MSI into spectral bases and representations, such that their spectral bases are shared and their representations are correlated with each other.

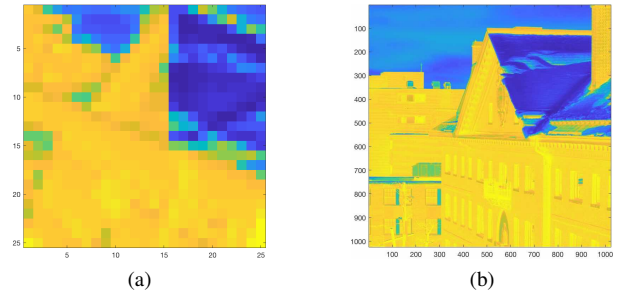


Fig. 2. Learned hidden representations from unregistered (a) low resolution HSI and (b) high resolution MSI, respectively, as shown in Fig. 1.

The novelty of this work is three-fold. First, the network extracts both the spectral and spatial information of two unregistered modalities through the same encoder-decoder structure, by projecting the LR HSI onto the same statistical space as HR MSI, as illustrated in Fig. 3. The representations of the network are encouraged to follow a Dirichlet distribution to naturally meet the non-negative and sum-to-one physical constraints. Second, to prevent spectral distortion, we further adopt mutual information (MI) to extract optimal and correlated representations from multi-modalities. Since the two-modalities are unregistered, the correlated representations are learned by maximizing the mutual information (MI) between the representations and their own inputs during the network optimization. Third, a collaborative l_{21} norm is employed as the reconstruction error instead of commonly used l_2 loss, so that the network is able to reconstruct individual pixels as accurately as possible. In this way, the network preserves the spectral information better. With the above design, the proposed network is able to work directly on unregistered

images and the spectral distortion of the reconstructed HR HSI can be largely reduced. The proposed method is referred to as unregistered and unsupervised mutual Dirichlet Net, or u^2 -MDN for short.

This work is an extension of our previous work uSDN [24]. However, uSDN only works on general Hyperspectral image super-resolution problem (HSI-SR) with well-registered LR HSI and HR MSI. Here, we have made substantial extensions to address the challenges of HSI-SR with unregistered multi-modalities. The major improvements are three-fold. First, instead of adopting two deep learning networks as uSDN, the proposed u^2 -MDN is specifically designed to extract the representations of multi-modalities with one encoder-decoder structure, which largely stabilized the network given unregistered multi-modalities. Second, uSDN minimizes spectral distortion of the reconstructed HR HSI by reducing the angular difference of the multi-modalities' representations, which fails to handle unregistered cases. While the proposed u^2 -MDN is able to handle both well-registered and unregistered cases by extracting correlated representations with mutual information(MI). Third, instead of commonly used l_2 loss adopted by uSDN, the collaborative l_{21} norm is introduced by the proposed u^2 -MDN to preserve the spectral information better.

II. RELATED WORK

A. Hyperspectral Image Super-Resolution

The problem of HSI-SR originates from multispectral image super-resolution (MSI-SR) in the remote sensing field, where the spatial resolution of MSI is further improved by a high-resolution panchromatic image (PAN). Traditional widely utilized MSI-SR methods can be roughly categorized into two groups: the component substitution (CS) and the multi-resolution analysis (MRA) based approaches. Generally, CS-based approaches [26] project the given data onto a predefined space where the spectral information and spatial information are separated. Subsequently, the spatial component is substituted with the one extracted from PAN [27], [29]. MRA based approaches achieve the spatial details by first applying a spatial filter to the HR images. Then the spatial details are injected into the LR HSI [28], [30], [66]–[69]. Although these traditional pan-sharpening approaches can be extended to solve the HSI-SR problem, they usually suffer from severe spectral distortions [21], [25], [30] as discussed in Sec. I.

Recent approaches consist of Bayesian based and matrix factorization based methods [8], [30]. Bayesian approaches estimate the posterior distribution of the HR HSI given LR HSI and HR MSI. The unique framework of Bayesian offers a convenient way to regularize the solution space of HR HSI by employing a proper prior distribution such as Gaussian. Different methods vary according to the different prior distributions adopted. Wei *et al.* proposed a Bayesian Naive method [70] based on the assumption that the representation coefficients of HR HSI follow a Gaussian distribution. However, this assumption does not always hold especially when the ground truth HR HSI contains complex textures. Instead of using Gaussian prior, dictionary based approaches solve the problem under the assumption that HR HSI is a linear combination

of properly chosen over-complete dictionary and sparse coefficients [34]. Simoes *et al.* proposed HySure [35], which takes into account both the spatial and spectral characteristics of the given data. This approach solves the problem through vector based total variation regularization. Akhtar *et al.* [21] introduced a non-parametric Bayesian strategy to solve the HSI-SR problem. The method first learns a spectral dictionary from LR HSI under the Bayesian framework. Then it estimates the spatial coefficients of the HR MSI by Bayesian sparse coding. Eventually, the HR HSI is generated by combining the spatial dictionary with the spatial coefficients.

Matrix factorization based approaches have been actively studied recently [20], [22], [31]–[33], with Kawakami *et al.* [20] being the first that introduced matrix factorization to solve the HSI-SR problem. The method learns a spectral basis from LR HSI and then use this basis to extract sparse coefficients from HR MSI with non-negative constraints. Similar to Bayesian based approaches, the HR HSI is generated by linearly combining the estimated bases with the coefficients. Yokoya *et al.* [32] decomposed both the LR HSI and HR MSI alternatively to achieve the optimal non-negative bases and coefficients that used to generate HR HSI. Wycoff *et al.* [71] solved the problem with alternating direction method of multipliers (ADMM). Lanaras *et al.* [22] further improved the fusion results by introducing a sparse constraint. However, most methods [22], [32], [71] are based on the same assumption that the down-sampling function between the spatial coefficients of HR HSI and LR HSI is known beforehand. This assumption is not always true.

B. Deep learning based Super-Resolution

Deep learning attracts increasing attention for natural image super-resolution since 2014, when Dong *et al.* first introduced convolution neural network (CNN) to solve the problem of natural image super-resolution and demonstrated state-of-the-art restoration quality [72]. Ledig *et al.* proposed a method based on generative adversarial network and skipped residual network [43]. The method employed perceptual loss through VGG network [73], [74] which is able to recover photo-realistic textures from heavily down-sampled images [41]. Usually, natural image SR methods only works up to 8 times upscaling. There have been several attempts to address the MSI-SR or HSI-SR with deep learning in a supervised fashion. In 2015, a modified sparse tied-weights denoising autoencoder was proposed by Huang *et al.* [52] to enhance the resolution of MSI. The method assumes that the mapping function between LR and HR PAN are the same as the one between LR and HR MSI. Masi *et al.* proposed a supervised three-layer SR-CNN [53] to learn the mapping function between LR MSI and HR MSI. Similar to [53], Wei *et al.* [54] learned the mapping function with deep residual network [43]. Li *et al.* [75] solved the HSI-SR problem by learning a mapping function with spatial constraint strategy and convolutional neural network. Dian *et al.* [76] initialized the HR HSI from the fusion framework via Sylvester equation. Then, the mapping function is trained between the initialized HR-HSI and the reference HR HSI through deep residual learning. However, these deep

learning based methods can not be readily adopted on HSI-SR due to the reasons elaborated in Sec. I.

Recently, we proposed an unsupervised uSDN [24], which addressed the problem of HSI-SR with deep network models. Specifically, it extracts the spectral and spatial information through two encoder-decoder networks from the two modalities. The angular difference between the LR HSI and HR MSI representations is minimized to reduce the spectral distortion for every ten iterations. However, the method only works for well registered images.

III. PROBLEM FORMULATION

Given the LR HSI, $\bar{\mathbf{Y}}_h \in \mathbb{R}^{m \times n \times L}$, where m , n and L denote its width, height and number of spectral bands, respectively, and the unregistered HR MSI with overlapped region, $\bar{\mathbf{Y}}_m \in \mathbb{R}^{M \times N \times l}$, where M , N and l denote its width, height and number of spectral bands, respectively, the goal is to reconstruct the HR HSI $\bar{\mathbf{X}} \in \mathbb{R}^{M \times N \times L}$ based on the content of HR MSI. In general, MSI has much higher spatial resolution than HSI, and HSI has much higher spectral resolution than MSI, *i.e.*, $M \gg m$, $N \gg n$ and $L \gg l$.

To facilitate the subsequent processing, we unfold the 3D images into 2D matrices, $\mathbf{Y}_h \in \mathbb{R}^{mn \times L}$, $\mathbf{Y}_m \in \mathbb{R}^{MN \times l}$ and $\mathbf{X} \in \mathbb{R}^{MN \times L}$, such that each row represents the spectral reflectance of a single pixel. Since each pixel in both LR HSI and HR MSI can be approximated by a linear combination of c spectral bases \mathbf{D} [21], [22], [24], the matrices can be further decomposed as

$$\mathbf{Y}_h = \mathbf{S}_h \mathbf{D}_h \quad (1)$$

$$\mathbf{Y}_m = \mathbf{S}_m \mathbf{D}_m \quad (2)$$

$$\mathbf{X} = \mathbf{S}_m \mathbf{D}_h \quad (3)$$

where $\mathbf{D}_h \in \mathbb{R}^{c \times L}$, $\mathbf{D}_m \in \mathbb{R}^{c \times l}$ denote the spectral bases of LR HSI and HR MSI, respectively. And $\mathbf{S}_h \in \mathbb{R}^{mn \times c}$, $\mathbf{S}_m \in \mathbb{R}^{MN \times c}$ denote the coefficients of LR HSI and HR MSI, respectively. Since \mathbf{S}_h or \mathbf{S}_m indicate how the spectral bases are combined for individual pixels at specific locations, they preserve the spatial structure of HSI. Note that the benefit of unfolding the data into 2D matrices is that, the extracting procedure can decouple each pixel without changing the relationship of the pixel and its neighborhood pixels, thus the reconstructed image has less artifacts [21], [22], [24].

In real applications, although the areas captured by LR HSI and HR MSI might not be registered well, they always have overlapping regions, and the LR HSI includes all the spectral basis of HR MSI *i.e.*, they share the same type of materials carrying specific spectral signatures. The relationship between LR HSI and HR MSI can be expressed as

$$\mathcal{C}_h \neq \mathcal{C}_m, \quad \mathcal{C}_h \cap \mathcal{C}_m \neq \emptyset, \quad \mathbf{D}_m = \mathbf{D}_h \mathcal{R}, \quad (4)$$

where \mathcal{C}_h and \mathcal{C}_m denote the contents of LR HSI and HR MSI, respectively. $\mathcal{R} \in \mathbb{R}^{L \times l}$ is the prior transformation matrix of sensor [20], [22]–[25], [30], [32], [34], [35], which describes the relationship between HSI and MSI bases.

With $\mathbf{D}_h \in \mathbb{R}^{c \times L}$ carrying the high-resolution spectral information and $\mathbf{S}_m \in \mathbb{R}^{MN \times c}$ carrying the high-resolution

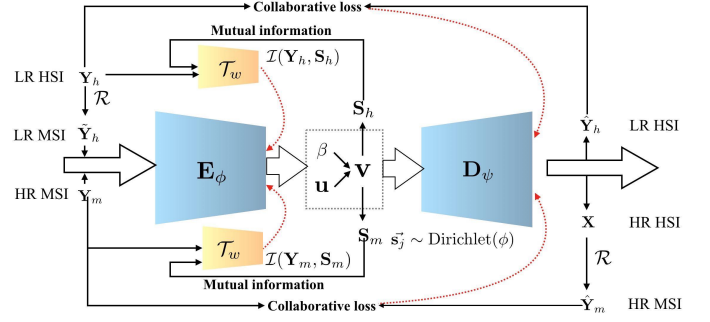


Fig. 3. Simplified architecture of u^2 -MDN.

spatial information, the desired HR HSI, \mathbf{X} , is generated by Eq. (3).

The challenges to solve this problem is that 1) the ground truth \mathbf{X} is not available, and 2) the LR HSI and HR MSI do not cover the same region. To solve this unsupervised and unregistered HR-HSI problem, the key is to take advantage of the shared spectral information \mathbf{D}_h among different modalities. In addition, the representations of both modalities specifying the spatial information of scene should meet the non-negative and sum-to-one physical constraints. Moreover, in the ideal case, for the pixels in the overlapped region between LR HSI and HR MSI, their spatial information should follow similar patterns, because they carry the information of how the reflectance of shared materials (spectral basis) are mixed in each location. Therefore, the network should have the ability to learn correlated spatial and spectral information from unregistered multi-modality images to maximize its ability to prevent spectral distortion.

IV. PROPOSED APPROACH

We propose an unsupervised architecture for unregistered LR HSI and HR MSI as shown in Fig. 3. Here, we highlight the structural uniquenesses of the network. To extract correlated spectral and spatial information of unregistered multi-modalities, the network projects the LR HSI into the same statistical space as HR MSI, so that the two modalities can share the same encoder and decoder. The encoder enforces the representations (carrying spatial information) of both modalities to follow a Dirichlet distribution, to naturally meet the non-negative and sum-to-one physical properties. In order to prevent spectral distortion, mutual information is introduced during optimization to maximize the correlation between the representations of LR HSI and HR MSI. And the collaborative l_{21} loss is adopted to encourage the network to extract accurate spectral and spatial information from both modalities.

A. Network Architecture

As shown in Fig. 3, the network reconstructs both the LR HSI \mathbf{Y}_h and HR MSI \mathbf{Y}_m by sharing the same encoder and decoder network structure. Since the number of the spectral band L of the HSI \mathbf{Y}_h is much larger than that of the spectral band l of MSI \mathbf{Y}_m , we project \mathbf{Y}_h into an l dimensional space by $\hat{\mathbf{Y}}_h = \mathbf{Y}_h \mathcal{R}$, such that $\hat{\mathbf{Y}}_h$ represents the LR MSI lying in the same space as HR MSI. In this way, both modalities are

linked to share the same encoder structure without additional parameters.

On the other hand, the spectral information \mathbf{D}_m of MSI is highly compressed from that of HSI, *i.e.*, $\mathbf{D}_m = \mathbf{D}_h \mathcal{R}$. Thus, it is very unstable and difficult to directly extract \mathbf{D}_h , carrying high spectral resolution from, MSI with low-spectral resolution. But the spectral basis of HR MSI can be transformed from those of LR HSI which possesses more spectral information, *i.e.*, $\hat{\mathbf{Y}}_m = \mathbf{S}_m \mathbf{D}_m = \mathbf{S}_m \mathbf{D}_h \mathcal{R} = \mathbf{X} \mathcal{R}$. Therefore, in the network design, both modalities share the same decoder structure \mathbf{D}_h . And the transformation matrix \mathcal{R} is added as fixed weights to reconstruct the HR MSI $\hat{\mathbf{Y}}_m$. Then the output of the layer before the fixed weights is actually \mathbf{X} , according to Eq. (3).

Let us define the input domain as $\mathcal{Y} = \{\tilde{\mathbf{Y}}_h, \mathbf{Y}_m\}$, output domain as $\hat{\mathcal{Y}} = \{\hat{\mathbf{Y}}_h, \mathbf{X}\}$, and the representation domain as $\mathcal{S} = \{\mathbf{S}_h, \mathbf{S}_m\}$, the encoder of the network $\mathbf{E}_\phi : \mathcal{Y} \rightarrow \mathcal{S}$, maps the input data to low-dimensional representations (latent variables on the Bottleneck hidden layer), *i.e.*, $p_\phi(\mathcal{S}|\mathcal{Y})$ and the decoder $\mathbf{D}_\psi : \mathcal{S} \rightarrow \hat{\mathcal{Y}}$ reconstructs the data from the representations, *i.e.*, $p_\psi(\hat{\mathcal{Y}}|\mathcal{S})$. Note that the bottleneck hidden layer \mathcal{S} behaves as the representation layer that reflects the spatial information, and the weights ψ of the decoder \mathbf{D}_ψ serve as \mathbf{D}_h in Eq. (1), respectively. This correspondence is further elaborated below.

Taking the procedure of training LR HSI as an example. The LR HSI is reconstructed by $\hat{\mathbf{Y}}_h = \mathbf{D}_\psi(\mathbf{S}_h)$, where $\mathbf{S}_h = \mathbf{E}_\phi(\mathbf{Y}_h)$. Since \mathbf{Y}_h carries the high-resolution spectral information, to better extract the spectral basis, part of the network should simulate the prior relationship described in Eq. (1). That is, the representation layer \mathbf{S}_h acts as the proportional coefficients and the weights ψ of the decoder correspond to the spectral basis \mathbf{D}_h in Eq. (1). Therefore, in the network structure, we define $\psi = \mathbf{W}_1 \mathbf{W}_2 \dots \mathbf{W}_k = \mathbf{D}_h$ with identity activation function without bias, where \mathbf{W}_k denotes the weights in the k th layer. In this way, \mathbf{D}_h preserves the spectral information of LR HSI, and the latent variables \mathbf{S}_h preserves the spatial information effectively. More implementation details will be described in Sec. IV-B.

Eventually, the desired HR HSI is generated directly by $\mathbf{X} = \mathbf{S}_m \mathbf{D}_h$. Note that the dashed lines in Fig. 3 show the path of back-propagation which will be elaborated in Sec. IV-C.

B. Mutual Dirichlet Network with Collaborative Constraint

To extract better spectral information and naturally incorporate the physical requirements of spatial information, *i.e.*, non-negative and sum-to-one, the representations \mathcal{S} are encouraged to follow a Dirichlet distribution. In addition, the network should have the ability to learn the correlated and optimized representations generated from the encoder \mathbf{E}_ϕ for both modalities. Thus, in the network design, we maximize the mutual information (MI) between the representations of LR HSI, \mathbf{S}_h , and HR MSI, \mathbf{S}_m , by maximizing the MI between the input images and their own representations. To further reduce the spectral distortion, the collaborative $l_{2,1}$ loss is incorporated into the network instead of traditional l_2 reconstruction loss. The detailed encoder-decoder structure and the MI structure are shown in Fig. 4 and Fig. 5, respectively.

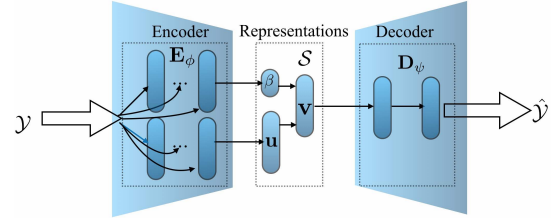


Fig. 4. Details of the encoder-decoder structure.

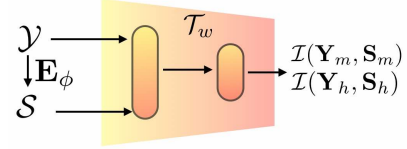


Fig. 5. Details of the MI structure.

1) *Dirichlet Structure*: To generate representations with Dirichlet distribution, we incorporate the stick-breaking structure between the encoder and representation layers. The stick-breaking process was first proposed by Sethuranman [77] back in 1994. It can be illustrated as breaking a unit-length stick into c pieces, the length of which follows a Dirichlet distribution. Nalisnick and Smyth, and Qu *et al.* successfully coupled the expressiveness of networks with Bayesian nonparametric model through stick-breaking process [24], [78]. Here, we follow the work of [24], [78], which draw the samples of \mathcal{S} from Kumaraswamy distribution [79].

The stick-breaking process is integrated into the network between the encoder \mathbf{E}_ϕ and the decoder \mathbf{D}_ψ , as shown in Fig. 3. Assuming that the generated representation row vector is denoted as $\mathbf{s}_i = \{s_{ij}\}_{1 \leq j \leq c}$, we have $0 \leq s_{ij} \leq 1$, and $\sum_{j=1}^c s_{ij} = 1$. Each variable s_{ij} can be defined as

$$s_{ij} = \begin{cases} v_{i1} & \text{for } j = 1 \\ v_{ij} \prod_{k < j} (1 - v_{ik}) & \text{for } j > 1, \end{cases} \quad (5)$$

where $v_{ik} \sim \text{Beta}(u, \alpha, \beta)$. Since it is difficult to draw samples directly from Beta distribution, we draw samples from the inverse transform of Kumaraswamy distribution. The benefit of Kumaraswamy distribution is that it has a closed-form CDF, and it is equivalent to Beta distribution when $\alpha = 1$ or $\beta = 1$. Let $\alpha = 1$, we have

$$v_{ik} \sim 1 - (1 - u_{ik}^{\frac{1}{\beta_i}}). \quad (6)$$

Both parameters u_{ik} and β_i are learned through the network for each row vector as illustrated in Fig. 3. Because $\beta > 0$, a softplus is adopted as the activation function [80] at the β layer. Similarly, a sigmoid [81] is used to map u into $(0, 1)$ range at the \mathbf{u} layer. Due to the fact that the spectral signatures of data are different for each image pair, the network only trains one group of data, *i.e.*, LR HSI \mathbf{Y}_h and HR MSI \mathbf{Y}_m , to reconstruct its own HR HSI \mathbf{X} . Therefore, to increase the representation power of the network, the encoder of the network is densely connected, *i.e.*, each layer is fully connected with all its subsequent layers [82].

2) *Mutual Dirichlet Network*: Before further describing the details of the network, we first explain the reason that motivates this design. Given unregistered multi-modalities LR HSI, \mathbf{Y}_h and HR MSI, \mathbf{Y}_m , and the desired HR HSI, \mathbf{X} , each pixel of which indicates the mixed spectral reflection of the captured area. The overlapped region of the three modalities is defined by \mathcal{C} . Ideally, each pixel in the overlapped region of these three modalities should possess the same spectral signatures. In addition, the corresponding proportional coefficients of \mathbf{X} and \mathbf{Y}_m should be the same for a given pixel within \mathcal{C} . Since \mathbf{Y}_h is a down-sampling and transformed version of \mathbf{X} , its proportional coefficients (representations) should follow the same pattern as that of \mathbf{X} and \mathbf{Y}_m , *i.e.*, \mathbf{S}_h and \mathbf{S}_m should be highly correlated although with different resolution. One example is shown in Fig. 1. Therefore, to generate HR HSI with low spectral distortion, it is necessary to encourage the representations \mathbf{S}_h and \mathbf{S}_m to follow similar patterns. However, traditional constraints like correlation may not work properly, because the input LR HSI and HR MSI are not registered with each other and the mapping function \mathbf{E}_ϕ , between the input \mathcal{Y} and the representations \mathcal{S} , holds the non-linear property. Therefore, we introduce mutual information (MI), which captures the non-linear statistical dependencies between variables [83], to reinforce the representations of LR HSI and HR MSI to follow similar patterns with statistics.

Mutual information has been widely used for multi-modality registrations [84], [85]. It is a Shannon-entropy based measurement of mutual independence between two random variables, *e.g.*, \mathbf{S}_h and \mathbf{S}_m . The mutual information $\mathcal{I}(\mathbf{S}_h; \mathbf{S}_m)$ measures how much uncertainty of one variable (\mathbf{S}_h or \mathbf{S}_m) is reduced given the other variable (\mathbf{S}_m or \mathbf{S}_h). Mathematically, it is defined as

$$\begin{aligned} \mathcal{I}(\mathbf{S}_h; \mathbf{S}_m) &= H(\mathbf{S}_h) - H(\mathbf{S}_h | \mathbf{S}_m) \\ &= \int_{\mathcal{S}_h \times \mathcal{S}_m} \log \frac{d\mathbb{P}_{\mathbf{S}_h \mathbf{S}_m}}{d\mathbb{P}_{\mathbf{S}_h} d\mathbb{P}_{\mathbf{S}_m}} d\mathbb{P}_{\mathbf{S}_h \mathbf{S}_m} \end{aligned} \quad (7)$$

where H indicates the Shannon entropy, $H(\mathbf{S}_h | \mathbf{S}_m)$ is the conditional entropy of \mathbf{S}_h given \mathbf{S}_m . $d\mathbb{P}_{\mathbf{S}_h \mathbf{S}_m}$ is the joint probability distribution, and $\mathbb{P}_{\mathbf{S}_h}$, $\mathbb{P}_{\mathbf{S}_m}$ denote the marginals. Belghazi *et al.* [86] introduced an MI estimator, which allows neural network to estimate MI through back-propagation, by adopting the concept of Donsker-Varadhan representation [87].

In order to maximally preserve the spectral information of the reconstructed HR HSI, our goal is to encourage the two representations \mathbf{S}_h and \mathbf{S}_m to follow similar patterns by maximizing their mutual information (MI), $\mathcal{I}(\mathbf{S}_h; \mathbf{S}_m)$, during optimization procedure. Since $\mathbf{S}_h = \mathbf{E}_\phi(\mathbf{Y}_h)$ and $\mathbf{S}_m = \mathbf{E}_\phi(\mathbf{Y}_m)$, the MI can also be expressed as $\mathcal{I}(\mathbf{E}_\phi(\mathbf{Y}_h); \mathbf{E}_\phi(\mathbf{Y}_m))$. However, it is difficult to maximize such MI directly with neural network, because the two modalities do not match with each other in our scenario. Therefore, we maximize the average MI between the representations and their own inputs, *i.e.*, $\mathcal{I}(\mathbf{Y}_h, \mathbf{E}_\phi(\mathbf{Y}_h))$ and $\mathcal{I}(\mathbf{Y}_m, \mathbf{E}_\phi(\mathbf{Y}_m))$. The benefit of doing this is two-fold. First, by optimizing the encoder weights \mathbf{E}_ϕ , it is able to greatly improve the quality of individual representations [88]. Thus it helps the network preserve the spectral and spatial information better. Second, since the multi-modalities are correlated, and the dependencies (MI) between

the representations and multi-modalities are maximized, it also maximizes the MI, $\mathcal{I}(\mathbf{S}_h; \mathbf{S}_m)$, between different modalities, such that \mathbf{S}_h and \mathbf{S}_m are encouraged to follow similar patterns.

Taking $\mathcal{I}(\mathbf{Y}_h, \mathbf{E}_\phi(\mathbf{Y}_h))$ as an example. It is equivalent to Kullback-Leibler (KL) divergence [86] between the joint distribution $\mathbb{P}_{\mathbf{Y}_h \mathbf{E}_\phi(\mathbf{Y}_h)}$ and the product of the marginals $\mathbb{P}_{\mathbf{Y}_h} \otimes \mathbb{P}_{\mathbf{E}_\phi(\mathbf{Y}_h)}$. Let $\mathbb{P} = \mathbb{P}_{\mathbf{Y}_h \mathbf{E}_\phi(\mathbf{Y}_h)}$ and $\mathbb{Q} = \mathbb{P}_{\mathbf{Y}_h} \otimes \mathbb{P}_{\mathbf{E}_\phi(\mathbf{Y}_h)}$, we can further express MI as

$$\mathcal{I}(\mathbf{Y}_h, \mathbf{E}_\phi(\mathbf{Y}_h)) = \mathbb{E}_{\mathbb{P}}[\log \frac{d\mathbb{P}}{d\mathbb{Q}}] = D_{KL}(\mathbb{P} \parallel \mathbb{Q}) \quad (8)$$

Such MI can be maximized by maximizing the KL-divergence's lower bound based on Donsker-Varadhan (DV) representation [87]. Since we do not need to calculate the exact MI, we introduce an alternative lower bound based on Jensen-Shannon which works better than DV based objective function [88].

In the network design, an additional network $\mathcal{T}_w : \mathcal{Y} \times \mathcal{S} \rightarrow \mathbb{R}$ is built with parameter w . Then the estimator can be defined as

$$\mathcal{I}_{\phi, w}(\mathbf{Y}_h, \mathbf{E}_\phi(\mathbf{Y}_h)) : = \mathbb{E}_{\mathbb{P}}[-sp(-\mathcal{T}_{w, \phi}(\mathbf{Y}_h, \mathbf{E}_\phi(\mathbf{Y}_h)))] \quad (9)$$

where $sp(x) = \log(1 + e^x)$. Note that we ignore the negative samples in DV based objective function [88], which are usually generated by shuffling the input data. Because it is unstable to train the network with random shifting input data given only two input data pairs. Since both \mathbf{E}_ϕ and \mathcal{T}_w are used to find the optimal representations, they are updated together. Combined with the MSI MI, the objective function is defined as

$$\begin{aligned} \mathcal{L}_{\mathcal{I}}(\phi, w) &= \mathcal{I}_{\phi, w}(\mathbf{Y}_h, \mathbf{E}_\phi(\mathbf{Y}_h)) \\ &\quad + \mathcal{I}_{\phi, w}(\mathbf{Y}_m, \mathbf{E}_\phi(\mathbf{Y}_m)) \end{aligned} \quad (10)$$

Since the encoder \mathbf{E}_ϕ and the estimation network of MI \mathcal{T}_w for both LR HSI and HR MSI share the same weights ϕ and w , their optimized representations follow similar patterns. More optimization details are described in Sec. IV-C.

In order to extract better spectral information, we adopt the collaborative reconstruction loss with $l_{2,1}$ norm [89] instead of traditional l_2 norm for both LR HSI and HR MSI. The objective function for $l_{2,1}$ loss is defined as

$$\begin{aligned} \mathcal{L}_{2,1}(\phi, w) &= \|D_\psi(E_\phi(\mathbf{Y}_h)) - \mathbf{Y}_h\|_{2,1} \\ &\quad + \|D_\psi(E_\phi(\mathbf{Y}_m)) - \mathbf{Y}_m\|_{2,1} \end{aligned} \quad (11)$$

where $\|X\|_{2,1} = \sum_{i=1}^m \sqrt{\sum_{j=1}^n X_{i,j}^2}$. $l_{2,1}$ norm will encourage the rows of the reconstruction error to be sparse. That is, the network is designed to learn individual pixels as accurate as possible. In this way, it extracts better spectral information and further reduces the spectral distortion.

C. Optimization and Implementation Details

The objective functions of the proposed network architecture can then be expressed as:

$$\mathcal{L}(\phi, w) = \mathcal{L}_{2,1}(\phi, w) - \lambda \mathcal{L}_{\mathcal{I}}(\phi, w) + \mu \|\psi\|_F^2 \quad (12)$$

where l_2 norm is applied on the decoder weights ψ to prevent over-fitting. λ and μ are the parameters that balance the trade-off between construction error, negative of mutual information and weights loss, respectively.

Before feeding into the network, the spectral vectors in LR HSI and HR MSI are transformed to zero-mean vectors by reducing the vector mean of their own image. Since the spectral information of MSI has been compressed too much (e.g., HSI has 31 bands, but MSI has 3 bands), the decoder of the network is only updated by LR HSI data to stabilize the network. The number of the input nodes is equal to the band number of HR MSI l . LR HSI \mathbf{Y}_h is projected into a l dimensional space by $\hat{\mathbf{Y}}_h = \mathbf{Y}_h \mathcal{R}$ before feeding into the network, while HR MSI is directly fed into the network. The number of the output nodes is chosen based on the band number of LR HSI L . When the input of the network is $\hat{\mathbf{Y}}_h$, the output of the decoder is $\hat{\mathbf{Y}}_h$. When the input of the network is \mathbf{Y}_m , the reconstructed $\hat{\mathbf{Y}}_m$ is generated by multiplying the output of the decoder with fixed weights \mathcal{R} .

The \mathbf{v} is drawn with Eq. (6) given \mathbf{u} and β , which are learned by back-propagation. β has only one node, which is learned by a two-layer densely-connected neural network. It denotes the distribution parameter of each pixel. u has 15 nodes, which are learned by a four-layer densely-connected neural-network. The representation layer \mathcal{S} with 15 nodes is constructed with \mathbf{v} and β , according to Eq. (5). The decoder and MI network \mathcal{T}_w have two fully-connected layers. The number of nodes and the activation functions for different layers are shown in Table. I.

The training is done in an unsupervised fashion without ground truth HR HSI. Given multi-modalities LR HSI and HR MSI, the network is optimized with back-propagation to extract their correlated spectral bases and representations, as illustrated in Fig. 3 with red-dashed lines. It stops when the reconstruction error of the network does not decrease anymore. Then we can feed the HR MSI into the network, and get the reconstructed HR HSI \mathbf{X} from the output of the decoder.

TABLE I
THE NUMBER OF LAYERS AND NODES IN THE PROPOSED NETWORK.

	encoder of \mathbf{u}/β	$\mathbf{u}/\beta/\mathbf{v}$	\mathcal{T}_w	decoder
#layers	4/2	1/1/1	2	2
#nodes	[3,3,3,3]/[3,3]	15/1/15	[18,1]	[15,15]
activation	linear	sigmoid/softplus/linear	sigmoid	linear

V. EXPERIMENTS AND RESULTS

A. Datasets and Experimental Setup

The proposed u^2 -MDN has been extensively evaluated with two widely used benchmark datasets, CAVE [90] and Harvard [1]. The CAVE dataset consists of 32 HR HSI images and each of which has a dimension of 512×512 with 31 spectral bands taken within the wavelength range $400 \sim 700\text{nm}$ at an interval of 10 nm. The Harvard dataset includes 50 HR HSI images with both indoor and outdoor scenes. The images are cropped to 1024×1024 , with 31 bands taken at an interval of 10nm within the wavelength range of $420 \sim 720\text{nm}$.

For real applications, the two modalities may be unregistered and the scale difference between the real LR HSI and HR HSI may be 10 or even more [57], [58]. However, not

all the approaches can reconstruct HR HSI from unregistered LR HSI and HR MSI. Thus, for fair comparison, we first evaluate the performance on individual well-registered image pairs with extreme super-resolution (sr) factor 32, where the LR HSI \mathbf{Y}_h is obtained by averaging the HR HSI over 32×32 disjoint blocks. The HR MSI with 3 bands are generated by multiplying the HR HSI with the given spectral response matrix \mathcal{R} of Nikon D700 [21], [22], [24].

The results of the proposed method on individual images in Fig. 6 are compared with eight state-of-the-art methods, i.e., traditional methods: CS based [29], MRA based methods: SFIM [68] and GLP [28]; Matrix factorization based methods: CNMF [32], Lanaras's (CSU) [22]; Bayesian based methods: HySure [35] and Akhtar's (BSR) [21]; and deep-learning based uSDN [24] that belong to different categories of HSI-SR. These methods also reported the best performance [21], [22], [24], [30], with the original code made available by the authors. The average results on the complete dataset is also reported to evaluate the robustness of the proposed method.

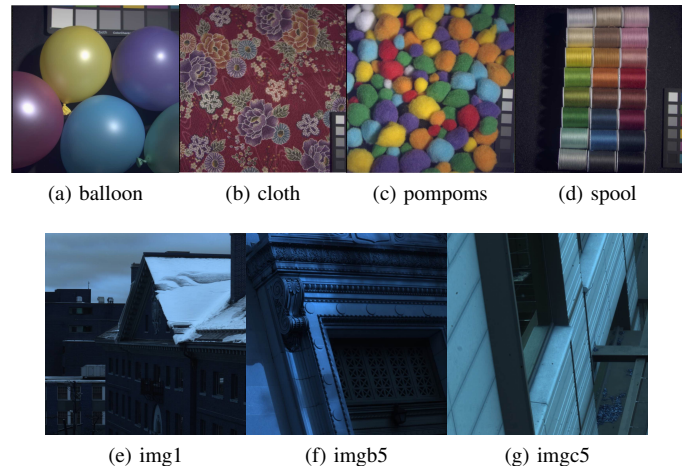


Fig. 6. The HR MSI of individual test images from the CAVE [90] (top row) and Harvard [1] (bottom row) datasets.

To further validate the effectiveness of the proposed approach, the performance on unregistered image pairs are reported. The unregistered image pairs are generated by rotating LR HSI with 5° and cropping 15% of its surrounding pixels, e.g., for images in the Cave dataset, 39322 pixels of the MSI are not covered in the LR HSI, for images in the Harvard dataset, 157290 pixels of the MSI are not covered in the LR HSI. Since only four methods that extract spectral information and spatial information independently may reconstruct HR HSI from unregistered images, the proposed method is compared with these four state-of-the-art methods, i.e., CS [29], SFIM [68], CNMF [32] and Akhtar's (BSR) [21]. Note that, in order to work on unregistered image pairs, the LR HSI should include all the spectral basis of HR MSI. Since not all the images can meet this requirement after rotation and cropping, we choose seven commonly benchmarked image pairs for comparison, as shown in Fig. 6.

B. Evaluation Metrics

For quantitative comparison, the erreur relative globale adimensionnelle de synthese (ERGAS), the peak signal-to-noise ratio (PSNR), and the spectral angle mapper (SAM) are applied to evaluate the quality of the reconstructed HSI.

ERGAS provides a measurement of band-wise normalized root of mean square error (RMSE) between the reference HSI, \mathbf{X} , and the reconstructed HSI, $\hat{\mathbf{X}}$, with the best value at 0 [91]. It is defined as

$$\text{ERGAS}(\mathbf{X}, \hat{\mathbf{X}}) = \frac{100}{\text{sr}} \sqrt{\frac{1}{L} \sum_{i=1}^L \frac{\text{mean}\|\mathbf{X}_i - \hat{\mathbf{X}}_i\|_2^2}{(\text{mean}\mathbf{X}_i)^2}}, \quad (13)$$

where sr denotes the sr factor between the HR MSI and LR HSI, L denotes the number of spectral bands of the reconstructed $\hat{\mathbf{X}}$.

PSNR is the average ratio between the maximum power of the image and the power of the residual errors in all the spectral bands. A larger PSNR indicates a higher spatial quality of the reconstructed HSI. For each image band of HSI, the PSNR is defined as

$$\text{PSNR}(\mathbf{X}_i, \hat{\mathbf{X}}_i) = 10 \cdot \log_{10} \left(\frac{\max(\mathbf{X}_i)^2}{\text{mean}\|\mathbf{X}_i - \hat{\mathbf{X}}_i\|_2^2} \right) \quad (14)$$

SAM [92] is commonly used to quantify the spectral distortion of the reconstructed HSI. The larger the SAM, the worse the spectral distortion of the reconstructed HSI. For each HSI pixel $\hat{\mathbf{X}}_j$, the SAM is defined as

$$\text{SAM}(\mathbf{X}_j, \hat{\mathbf{X}}_j) = \arccos \left(\frac{\mathbf{X}_j^T \hat{\mathbf{X}}_j}{\|\mathbf{X}_j\|_2 \|\hat{\mathbf{X}}_j\|_2} \right) \quad (15)$$

And the global SAM is estimated by averaging the SAM over all the pixels in the entire image.

C. Experimental Results on Registered Image Pairs

For fair comparison, we first perform experiments on the general case when LR HSI and HR MSI are well registered. Tables II, III and IV show the experimental results of 7 groups of commonly benchmarked images from the CAVE and Harvard datasets [20], [21], [93]. Note that, in order to show how the method works in different scenario, the data is not normalized. Since the intensities of Harvard dataset are small, the ERGAS of the methods are generally smaller than that of the CAVE dataset.

We observe that traditional methods suffer from spectral distortion, thus could not achieve competitive performance. The matrix-based approach, CSU [22] works better than CNMF [32] on both CAVE and Harvard dataset. And both CSU and CNMF preserve spectral information better than the Bayesian based methods. The reason is that they could extract more correlated spatial coefficients from LR HSI and HR MSI with the given predefined down-sampling function. But for the applications with unknown down-sampling function, this prior would limit their ability to extract accurate spatial information from data with arbitrary distributions.

The Bayesian non-parametric based method BSR [21] outperforms HySure [35] by estimating the spectra through non-parametric learning. However, although it can achieve results

with relatively low reconstruction error, it could not preserve the spectral information well. That is because the spectral and spatial information are extracted separately during the optimization of BSR. Therefore, the extracted spectral bases from LR HSI may not be the optimized spectral bases for HR MSI. Then the representations extracted from two modalities are not correlated. Thus the reconstructed HR HSI would have large spectral distortion.

The deep learning based uSDN preserves spectral information better than that of BSR. However, it can only work on well registered images due to its network design with angular difference regularization. Based on the experiments, the proposed u^2 -MDN network powered by the mutual information and collaborative $l_{2,1}$ loss outperforms all of the other approaches in terms of ERGAS, PSNR and SAM, and it is quite stable for different types of input images.

The average of ERGAS, PSNR and SAM over the complete CAVE and Harvard dataset are reported in Table V, to further demonstrate the robustness of the proposed u^2 -MDN. We only compare the performance of matrix factorization based CSU, Bayesian based BSR, and deep learning based uSDN since they demonstrated better performance on well-registered images. We observe that CSU achieves better results than BSR due to the predefined down-sampling function, which is given as a prior. Although BSR can achieve relatively good ERGAS and PSNR scores, its SAM scores are not promising. Due to the fact that it estimates the spectral and spatial information independently, it may not find the optimal representations to recover the HR HSI. The deep learning based methods uSDN is comparable to CSU, and it can reduce the spectral distortion better than BSR. However, its optimization strategy limits its ability to further reduce the spectral distortion. The proposed approach consistently outperforms the other methods and achieves the state-of-the-art performance in terms of ERGAS, PSNR and SAM as reported in Table V. It is very effective in preserving the spectral signature of the reconstructed HR HSI, showing much improved performance especially on SAM on the CAVE data. To demonstrate the reconstruction performance in different spectral bands, the averaged PSNR on each wavelength is shown in Fig. 7. We can observe that, the proposed method consistently outperforms the other methods for all the spectral bands.

TABLE II
BENCHMARKED RESULTS IN TERMS OF ERGAS.

Methods	CAVE				Harvard		
	balloon	cloth	pompoms	spool	img1	imgb5	imgc5
CS	0.33	0.51	0.47	0.67	0.16	0.25	0.19
SFIM	0.59	0.54	3.76	2.93	0.23	0.29	0.23
GLP	0.39	0.52	0.49	0.71	0.22	0.27	0.21
CNMF	0.26	0.54	0.31	0.54	0.15	0.17	0.13
CSU	0.19	0.40	0.28	0.45	0.12	0.18	0.12
HySure	0.34	0.53	0.46	0.66	0.17	0.35	0.19
BSR	0.30	0.48	0.48	0.62	0.14	0.30	0.18
uSDN	0.20	0.35	0.25	0.40	0.12	0.16	0.11
u^2 -MDN	0.16	0.30	0.19	0.37	0.11	0.15	0.11

TABLE III
BENCHMARKED RESULTS IN TERMS OF PSNR.

Methods	CAVE				Harvard		
	balloon	cloth	pompoms	spool	img1	imgb5	imgc5
CS	36.12	30.51	31.78	36.61	37.41	36.06	36.02
SFIM	33.52	30.59	25.39	28.63	32.62	33.15	35.62
GLP	36.01	32.04	30.69	35.89	33.26	33.88	35.98
CNMF	39.27	30.52	35.45	37.28	37.25	39.06	38.49
CSU	41.52	33.47	36.81	39.64	39.12	39.01	39.05
HySure	37.12	30.24	32.56	35.79	36.43	36.44	36.99
BSR	39.37	31.70	33.05	37.45	38.88	36.95	36.46
uSDN	41.54	33.48	37.84	38.49	39.30	39.72	39.12
u^2 -MDN	43.59	34.85	39.12	40.08	40.97	39.76	39.19

TABLE IV
BENCHMARKED RESULTS IN TERMS OF SAM.

Methods	CAVE				Harvard		
	balloon	cloth	pompoms	spool	img1	imgb5	imgc5
CS	10.07	7.95	10.39	13.54	2.79	3.18	2.77
SFIM	11.45	7.25	12.89	19.71	2.89	3.52	2.84
GLP	10.25	7.39	11.09	13.51	2.99	3.29	2.80
CNMF	9.71	6.55	6.32	16.77	2.86	2.14	2.64
CSU	4.68	5.52	6.01	6.84	2.30	2.37	2.38
HySure	10.21	7.09	10.65	17.19	4.06	3.43	2.93
BSR	9.63	7.02	10.13	14.52	2.78	3.27	2.67
uSDN	4.56	4.16	5.43	13.01	2.27	2.10	2.58
u^2 -MDN	1.93	4.31	3.46	4.47	2.06	2.08	1.77

D. Experimental Results on Unregistered Image Pairs

To solve the problem of unregistered hyperspectral image super-resolution, the LR HSI should contain all the spectral bases in the HR MSI. Since one pixel in the LR HSI covers 1024 pixels in the HR MSI, when the LR HSI is rotated and cropped, certain spectral information contained in HR MSI is corrupted or missing. Thus, the reconstruction error is expected to be increased.

The performance of different methods on unregistered image pairs are reported in Tables VI, VII and VIII. Note that, only the methods, that are able to extract the spectral and spatial information separately, can work on unregistered images. Thus four methods are compared in the tables. Traditional CS-based and MTF-based methods fail in this scenario. That is because when the given two modalities are unregistered, the spatial details could not be directly added to improve the spatial resolution of LR HSI. The performance of CNMF drops largely for both datasets. The reason is that the adopted predefined down-sampling function will introduce significant spectral distortion when the LR HSI and HR MSI are unregistered. BSR works better than the other three approaches due to the fact that, it extracts spectral and spatial information

TABLE V
THE AVERAGE ERGAS, PSNR AND SAM SCORES OVER COMPLETE BENCHMARKED DATASETS.

Methods	CAVE			Harvard		
	ERGAS	PSNR	SAM	ERGAS	PSNR	SAM
CSU [22]	0.40	38.50	7.14	0.29	40.01	4.38
BSR [21]	0.53	36.24	13.23	0.30	38.43	4.49
uSDN [24]	0.36	38.96	6.95	0.28	40.15	4.28
u^2 -MDN	0.31	40.65	4.72	0.23	41.37	3.28

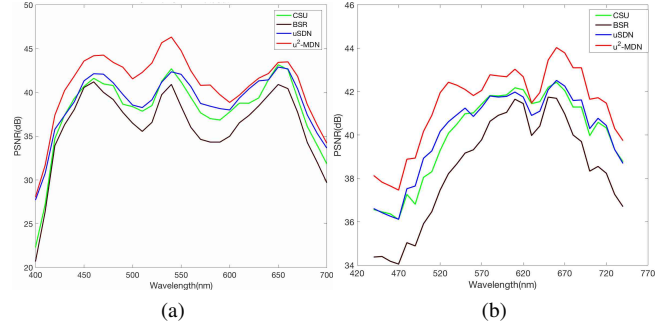


Fig. 7. The average PSNR of different wavelengths of the reconstructed HSI in the (a) CAVE dataset and (b) Harvard dataset, respectively.

separately with sparse constraints. However, the method could not preserve spectral information well, since the extracted spectral bases from LR HSI may not be the optimal bases to extract correlated spatial information from the HR MSI. The proposed u^2 -MDN is able to handle challenging scenarios much better than the state-of-the-art. The main reason that contributes to the success of the proposed approach is that, the network is able to extract the optimal and correlated spatial representations from two modalities through mutual information and collaborative loss. In this way, both the spatial and especially the spectral information are effectively preserved. This demonstrates the representation capacity of the proposed structure.

TABLE VI
RESULTS ON UNREGISTERED IMAGES IN TERMS OF ERGAS.

Methods	CAVE				Harvard		
	balloon	cloth	pompoms	spool	img1	imgb5	imgc5
CS	0.82	0.76	1.18	1.07	1.65	0.40	0.69
SFIM	1.51	1.01	1.82	1.88	1.33	0.68	0.89
CNMF	0.71	0.69	0.83	0.63	0.74	0.34	0.48
BSR	0.32	0.54	0.58	0.65	0.15	0.33	0.29
u^2 -MDN	0.30	0.40	0.37	0.56	0.13	0.25	0.14

TABLE VII
RESULTS ON UNREGISTERED IMAGES IN TERMS OF PSNR.

Methods	CAVE				Harvard		
	balloon	cloth	pompoms	spool	img1	imgb5	imgc5
CS	27.71	27.59	23.54	29.92	23.60	20.07	22.18
SFIM	22.47	24.74	19.50	25.30	17.41	25.38	19.93
CNMF	29.18	27.84	26.67	24.62	22.29	31.39	25.34
BSR	35.61	30.39	32.44	31.58	37.58	33.91	34.18
u^2 -MDN	38.61	32.89	33.64	36.25	39.42	36.90	36.29

To visualize the results, we show the reconstructed samples given unregistered image pairs of CAVE and Harvard datasets taken at wavelengths 420, 540, and 690 nm in Fig. 8. The first through fourth columns show the LR images, reconstructed images from our method, ground truth images, and the absolute difference between the images at the second and third columns, respectively.

We also compare the proposed method with other methods on the challenge images from CAVE and Harvard dataset. The results are shown in Figs. 9-11. We can observe from the absolute difference and SAM that, the results from CS and SFIM

TABLE VIII
RESULTS ON UNREGISTERED IMAGES IN TERMS OF SAM.

Methods	CAVE				Harvard		
	balloon	cloth	pompoms	spool	img1	imgb5	imgc5
CS	14.35	9.75	22.13	17.16	10.66	4.90	5.32
SFIM	12.69	9.65	14.89	21.02	3.28	4.44	3.96
CNMF	10.63	8.12	11.88	17.03	3.85	3.97	3.16
BSR	10.56	7.85	10.22	18.09	2.93	4.27	2.92
u^2 -MDN	3.48	6.08	4.87	6.78	2.32	2.73	2.26

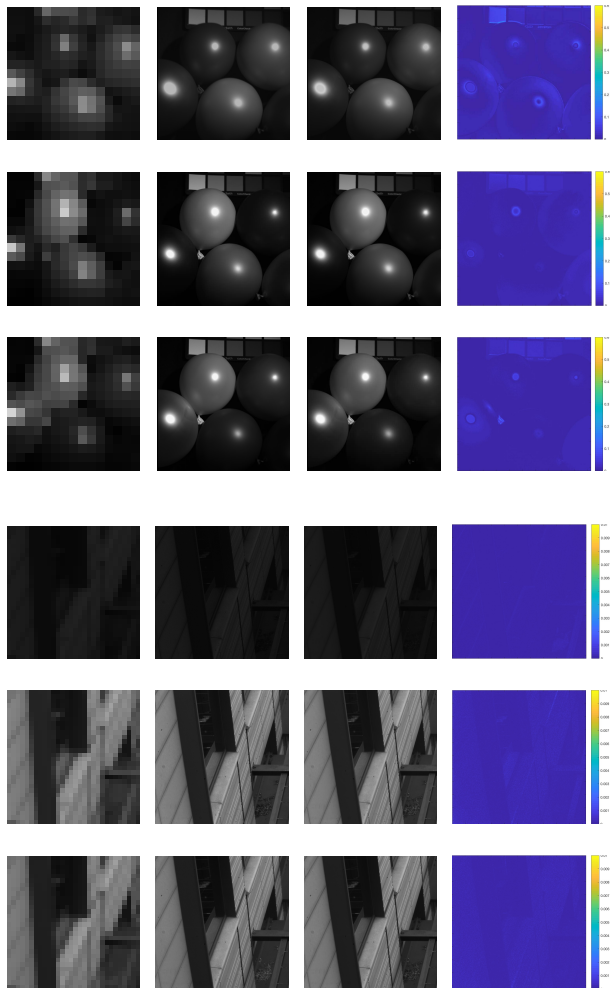


Fig. 8. Reconstructed images given unregistered LR HSI from the CAVE (top) and Harvard dataset (bottom) at wavelength 420, 540 and 690 nm. First column: LR images. Second: estimated images. Third: ground truth images. Fourth: absolute difference.

have large displacement since the LR HSI and HR MSI are not registered. The CNMF works slightly better, but it could not work effectively due to the predefined down-sampling function. The proposed method is comparable to BSR in terms of PSNR, but it has much less spectral distortion than that of BSR. In summary, the effectiveness of the proposed method can be readily observed from the difference images, SAM and PSNR, where the proposed approach is able to preserve both the spectral and spatial information.

E. Ablation and Parameter Study

Taking the challenging rotated ‘pompom’ image from the CAVE dataset as an example, we further evaluate 1) the necessity of maximizing the mutual information (MI) between representations and input images and 2) the usage of collaborative $l_{2,1}$ loss. Since they all designed to reduce the spectral distortion of the reconstructed image, we use SAM as the evaluation metric.

Fig. 12 illustrates the SAM of the reconstructed HR HSI when increasing the parameters of mutual information λ in Eq. 12. We can observe that, if there is no mutual information maximization, *i.e.* $\lambda = 0$, the spectral information would not be preserved well. When we gradually increase λ , the reconstructed HR HSI preserves better spectral information, *i.e.*, the SAM is largely reduced. The reason for that is, when we maximize the MI between the representations and their own inputs, it actually maximizes the mutual information of the representations of two modalities. Therefore, the network is able to correlate the extracted spectral and spatial information from unregistered HR MSI and LR MSI in an effective way, to largely reduce the spectral distortion. However, when the parameter is too large, it hinders the reconstruction procedure of the network. Therefore, we need to choose a proper λ for the network. In our experiments, we set $\lambda = 1 \times 10^{-5}$ and keep $\mu = 1 \times 10^{-4}$ during the experiments to reduce over-fitting.

The effectiveness evaluation of the collaborative l_{21} norm is demonstrated in Fig. 13. Because the l_{21} norm encourages the network to reconstruct individual pixels as accurately as possible, the network can preserve the spectral information better and significantly reduce the spectral distortion of the restored HR HSI.

F. Tolerance Study

At last, we would like to examine how much spectral information can be preserved when the network deals with unregistered images. To preserve spectral information, the input LR HSI should cover all the spectral signatures of HR MSI. Thus, we choose the image in Fig. 1 from the Harvard dataset which has most of spectral signatures centered in the image. The results are shown in Fig. 14. The image is rotated from 5 degrees to 30 degrees with 15% to 48% percents of information missing. We can observe that as long as the spectral bases are included in the LR HSI, no matter how small the overlapped region is between the LR HSI and HR MSI, we could always achieve the reconstructed image with small spectral distortion even for unregistered input images.

VI. CONCLUSION

We proposed an unsupervised encoder-decoder network u^2 -MDN to solve the problem of hyperspectral image super-resolution (HSI-SR) without multi-modality registration. The unique structure stabilizes the network training by projecting both modalities into the same space and extracting the spectral basis from LR HSI with rich spectral information as well as spatial representations from HR MSI with high-resolution spatial information simultaneously. The network learns correlated spatial information from two unregistered

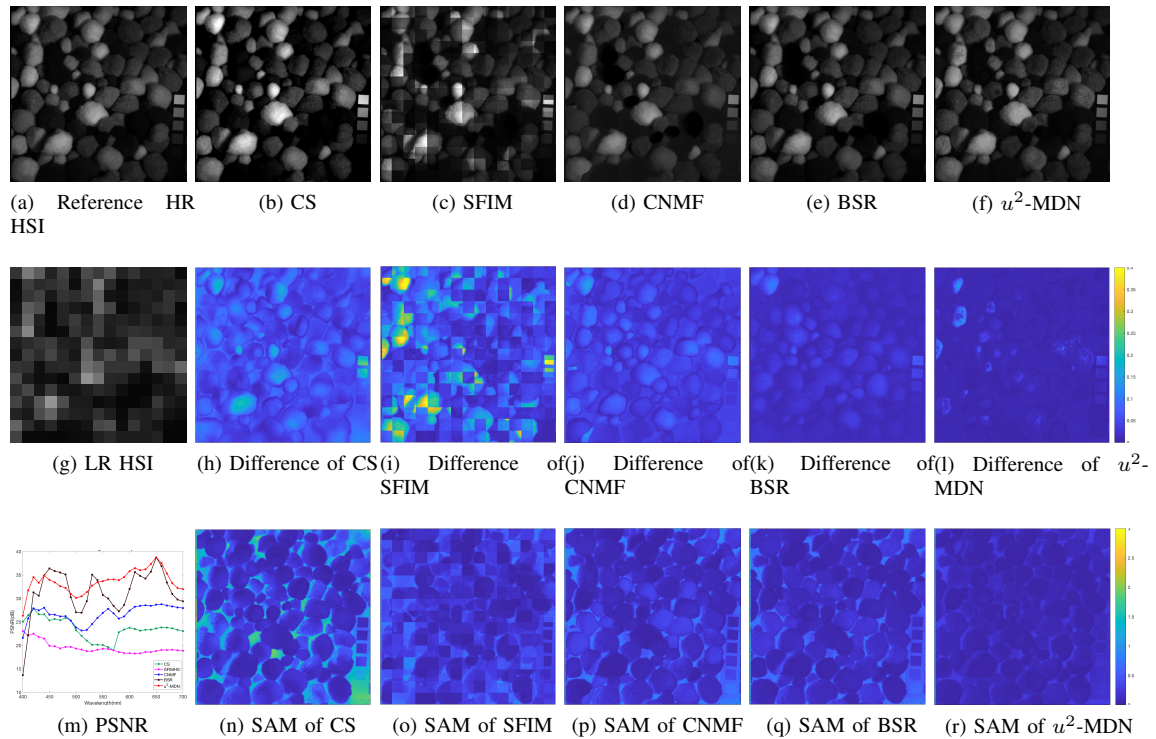


Fig. 9. Reconstructed results given unregistered image pairs from the CAVE dataset. (a) Reference HR HSI at wavelength 540 nm. (g) LR HSI at wavelength 540 nm. (b)-(f): reconstructed results at wavelength 540 nm from different methods. (h)-(l): average absolute difference between the reconstructed HSI and reference HSI over different spectral bands, from different methods. (n)-(r) SAM of each pixel between the reconstructed HSI and reference HSI from different methods. (m) PSNR of different methods.

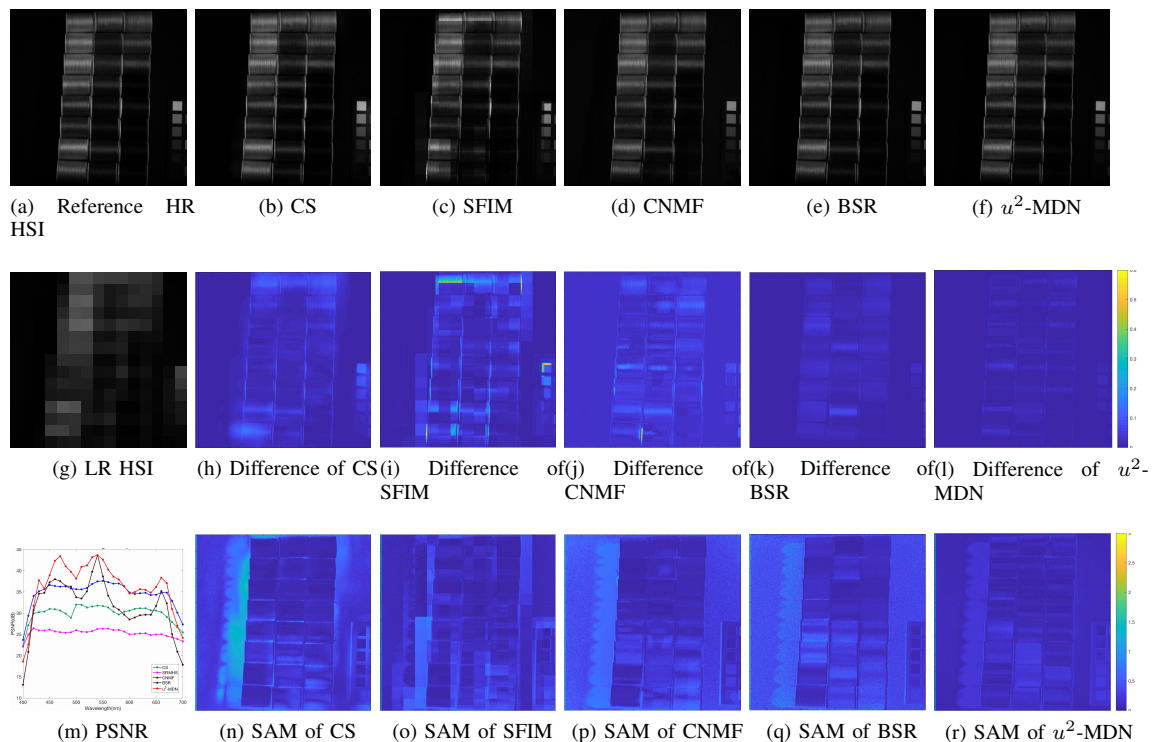


Fig. 10. Reconstructed results given unregistered image pairs from the CAVE dataset. (a) Reference HR HSI at wavelength 540 nm. (g) LR HSI at wavelength 540 nm. (b)-(f): reconstructed results at wavelength 540 nm from different methods. (h)-(l): average absolute difference between the reconstructed HSI and reference HSI over different spectral bands, from different methods. (n)-(r) SAM of each pixel between the reconstructed HSI and reference HSI from different methods. (m) PSNR of different methods.

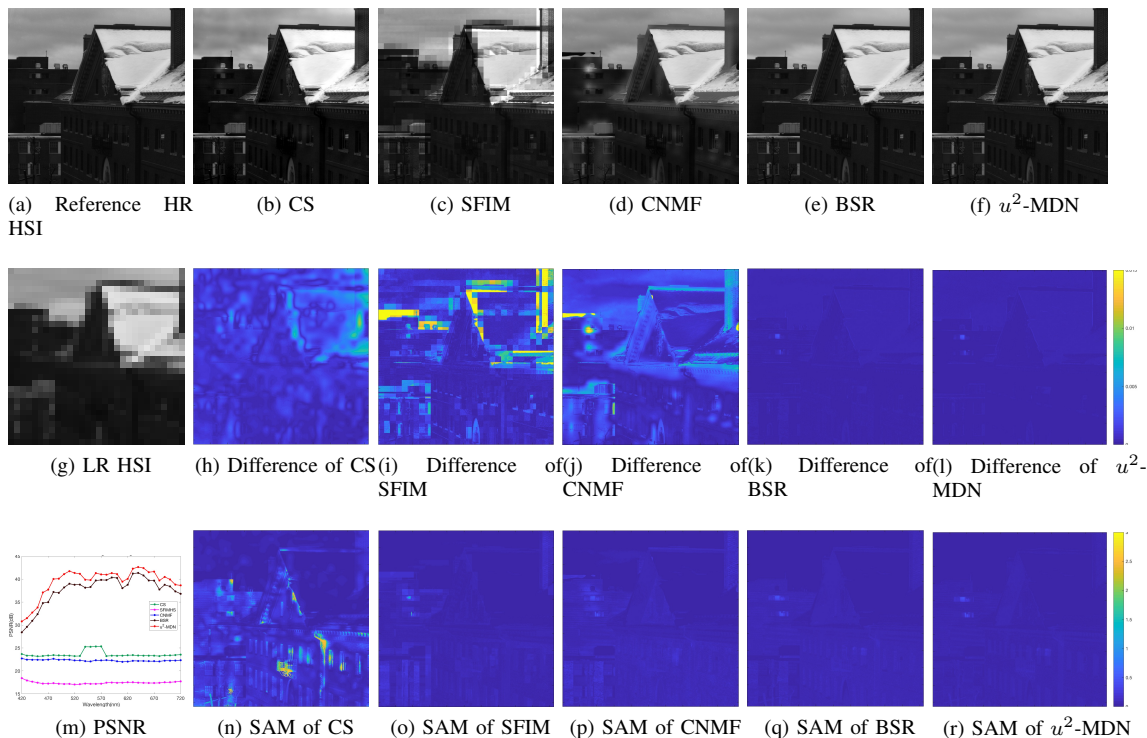


Fig. 11. Reconstructed results given unregistered image pairs from the Harvard dataset. (a) Reference HR HSI at wavelength 540 nm. (g) LR HSI at wavelength 540 nm. (b)-(f): reconstructed results at wavelength 540 nm from different methods. (h)-(l): average absolute difference between the reconstructed HSI and reference HSI over different spectral bands, from different methods. (n)-(r) SAM of each pixel between the reconstructed HSI and reference HSI from different methods. (m) PSNR of different methods.

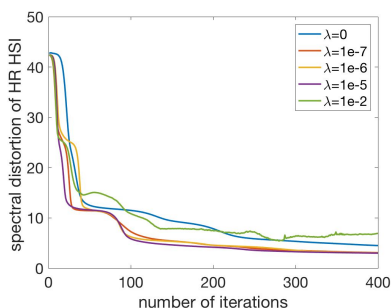


Fig. 12. Influence of MI

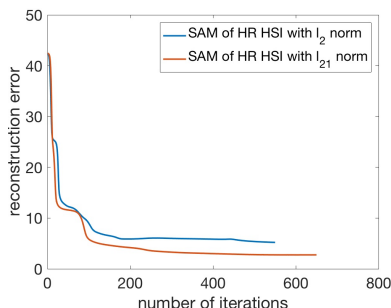


Fig. 13. The effect of l_{21}

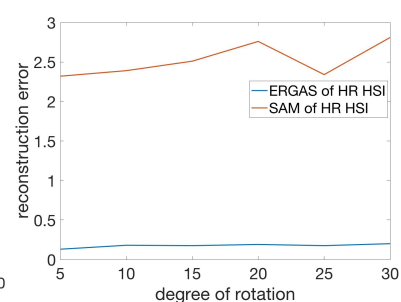


Fig. 14. Tolerance study

modalities by maximizing the mutual information (MI) between the representations and their own raw inputs. In this way, it maximizes the MI between the two representations that largely reduces the spectral distortion. In addition, the collaborative $l_{2,1}$ norm is adopted to encourage the network to further preserve spectral information. Extensive experiments on two benchmark datasets demonstrated the superiority of the proposed approach over state-of-the-art.

ACKNOWLEDGMENT

The authors would like to thank all the developers of the evaluated methods who kindly offer their codes. This publication was made possible in part by NASA grant NNX12CB05C and NNX16CP38P. The statements made herein are solely the responsibility of the authors.

REFERENCES

- [1] A. Chakrabarti and T. Zickler, "Statistics of real-world hyperspectral images," *The IEEE Conference on Computer Vision and Pattern Recognition (CVPR)*, pp. 193–200, 2011.
- [2] J. M. Bioucas-Dias, A. Plaza, N. Dobigeon, M. Parente, Q. Du, P. Gader, and J. Chanussot, "Hyperspectral unmixing overview: Geometrical, statistical, and sparse regression-based approaches," *Selected Topics in Applied Earth Observations and Remote Sensing, IEEE Journal of*, vol. 5, no. 2, 2012.
- [3] C. Kwan, B. Ayhan, G. Chen, J. Wang, B. Ji, and C.-I. Chang, "A novel approach for spectral unmixing, classification, and concentration estimation of chemical and biological agents," *IEEE Transactions on Geoscience and Remote Sensing*, vol. 44, no. 2, pp. 409–419, 2006.
- [4] M. Fauvel, Y. Tarabalka, J. A. Benediktsson, J. Chanussot, and J. C. Tilton, "Advances in spectral-spatial classification of hyperspectral images," *Proceedings of the IEEE*, vol. 101, no. 3, pp. 652–675, 2013.
- [5] F. Zhang, B. Du, and L. Zhang, "Scene classification via a gradient boosting random convolutional network framework," *IEEE Transactions on Geoscience and Remote Sensing*, vol. 54, no. 3, pp. 1793–1802, 2016.

- [6] E. Maggiori, G. Charpiat, Y. Tarabalka, and P. Alliez, "Recurrent neural networks to correct satellite image classification maps," *IEEE Transactions on Geoscience and Remote Sensing*, vol. 55, no. 9, pp. 4962–4971, Sept 2017.
- [7] M. Paoletti, J. Haut, J. Plaza, and A. Plaza, "A new deep convolutional neural network for fast hyperspectral image classification," *ISPRS Journal of Photogrammetry and Remote Sensing*, vol. 145, pp. 120–147, 2018.
- [8] N. Yokoya, C. Grohnfeldt, and J. Chanussot, "Hyperspectral and multispectral data fusion: A comparative review of the recent literature," *IEEE Geoscience and Remote Sensing Magazine*, vol. 5, no. 2, pp. 29–56, 2017.
- [9] J. M. Haut, M. E. Paoletti, J. Plaza, J. Li, and A. Plaza, "Active learning with convolutional neural networks for hyperspectral image classification using a new bayesian approach," *IEEE Transactions on Geoscience and Remote Sensing*, no. 99, pp. 1–22, 2018.
- [10] P. S. S. Ayday and S. Minz, "Classification of hyperspectral images using self-training and a pseudo validation set," *Remote Sensing Letters*, vol. 9, no. 11, pp. 1109–1117, 2018.
- [11] H. Van Nguyen, A. Banerjee, and R. Chellappa, "Tracking via object reflectance using a hyperspectral video camera," *IEEE Computer Society Conference on Computer Vision and Pattern Recognition Workshops (CVPRW)*, pp. 44–51, 2010.
- [12] Y. Fu, Y. Zheng, I. Sato, and Y. Sato, "Exploiting spectral-spatial correlation for coded hyperspectral image restoration," *The IEEE Conference on Computer Vision and Pattern Recognition (CVPR)*, June 2016.
- [13] B. UzKent, M. J. Hoffman, and A. Vodacek, "Real-time vehicle tracking in aerial video using hyperspectral features," *The IEEE Conference on Computer Vision and Pattern Recognition Workshops (CVPRW)*, June 2016.
- [14] B. UzKent, A. Rangnekar, and M. Hoffman, "Aerial vehicle tracking by adaptive fusion of hyperspectral likelihood maps," *The IEEE Conference on Computer Vision and Pattern Recognition Workshops (CVPRW)*, July 2017.
- [15] L. H. Spangler, L. M. Dobeck, K. S. Repasky, A. R. Nehrir, S. D. Humphries, J. L. Barr, C. J. Keith, J. A. Shaw, J. H. Rouse, A. B. Cunningham *et al.*, "A shallow subsurface controlled release facility in bozeman, montana, usa, for testing near surface co2 detection techniques and transport models," *Environmental Earth Sciences*, vol. 60, no. 2, pp. 227–239, 2010.
- [16] A. Plaza, Q. Du, J. M. Bioucas-Dias, X. Jia, and F. A. Kruse, "Foreword to the special issue on spectral unmixing of remotely sensed data," *IEEE Transactions on Geoscience and Remote Sensing*, vol. 49, no. 11, pp. 4103–4110, 2011.
- [17] H. Kwon and N. M. Nasrabadi, "Kernel matched signal detectors for hyperspectral target detection," *IEEE Computer Society Conference on Computer Vision and Pattern Recognition Workshops (CVPRW)*, pp. 6–6, 2005.
- [18] M. Borengasser, W. S. Hungate, and R. Watkins, *Hyperspectral remote sensing: principles and applications*, 2007.
- [19] M. S. M. Asaari, P. Mishra, S. Mertens, S. Dhondt, B. Inzé, N. Wuyts, and P. Scheunders, "Close-range hyperspectral image analysis for the early detection of stress responses in individual plants in a high-throughput phenotyping platform," *ISPRS Journal of Photogrammetry and Remote Sensing*, vol. 138, pp. 121–138, 2018.
- [20] R. Kawakami, Y. Matsushita, J. Wright, M. Ben-Ezra, Y.-W. Tai, and K. Ikeuchi, "High-resolution hyperspectral imaging via matrix factorization," *The IEEE Conference on Computer Vision and Pattern Recognition (CVPR)*, pp. 2329–2336, 2011.
- [21] N. Akhtar, F. Shafait, and A. Mian, "Bayesian sparse representation for hyperspectral image super resolution," *The IEEE Conference on Computer Vision and Pattern Recognition (CVPR)*, pp. 3631–3640, 2015.
- [22] C. Lanaras, E. Baltsavias, and K. Schindler, "Hyperspectral super-resolution by coupled spectral unmixing," *The IEEE Conference on Computer Vision and Pattern Recognition (CVPR)*, pp. 3586–3594, 2015.
- [23] G. Vivone, L. Alparone, J. Chanussot, M. Dalla Mura, A. Garzelli, G. A. Licciardi, R. Restaino, and L. Wald, "A critical comparison among pansharpening algorithms," *IEEE Transactions on Geoscience and Remote Sensing*, vol. 53, no. 5, 2015.
- [24] Y. Qu, H. Qi, and C. Kwan, "Unsupervised sparse dirichlet-net for hyperspectral image super-resolution," *The IEEE Conference on Computer Vision and Pattern Recognition (CVPR)*, pp. 2511–2520, 2018.
- [25] R. Dian, L. Fang, and S. Li, "Hyperspectral image super-resolution via non-local sparse tensor factorization," *The IEEE Conference on Computer Vision and Pattern Recognition (CVPR)*, pp. 5344–5353, 2017.
- [26] C. Thomas, T. Ranchin, L. Wald, and J. Chanussot, "Synthesis of multispectral images to high spatial resolution: A critical review of fusion methods based on remote sensing physics," *IEEE Transactions on Geoscience and Remote Sensing*, vol. 46, no. 5, pp. 1301–1312, 2008.
- [27] S. C. Sides, J. A. Anderson *et al.*, "Comparison of three different methods to merge multiresolution and multispectral data- landsat tm and spot panchromatic," *Photogrammetric Engineering and remote sensing*, vol. 57, no. 3, pp. 295–303, 1991.
- [28] B. Aiazzi, L. Alparone, S. Baronti, A. Garzelli, and M. Selva, "Mtf-tailored multiscale fusion of high-resolution ms and pan imagery," *Photogrammetric Engineering & Remote Sensing*, vol. 72, no. 5, pp. 591–596, 2006.
- [29] B. Aiazzi, S. Baronti, and M. Selva, "Improving component substitution pansharpening through multivariate regression of ms+ pan data," *IEEE Transactions on Geoscience and Remote Sensing*, vol. 45, no. 10, 2007.
- [30] L. Loncan, L. B. de Almeida, J. M. Bioucas-Dias, X. Briottet, J. Chanussot, N. Dobigeon, S. Fabre, W. Liao, G. A. Licciardi, M. Simoes *et al.*, "Hyperspectral pansharpening: a review," *IEEE Geoscience and Remote Sensing Magazine*, vol. 3, no. 3, 2015.
- [31] W. Dong, F. Fu, G. Shi, X. Cao, J. Wu, G. Li, and X. Li, "Hyperspectral image super-resolution via non-negative structured sparse representation," *IEEE Transactions on Image Processing*, vol. 25, no. 5, pp. 2337–2352, 2016.
- [32] N. Yokoya, T. Yairi, and A. Iwasaki, "Coupled nonnegative matrix factorization unmixing for hyperspectral and multispectral data fusion," *IEEE Transactions on Geoscience and Remote Sensing*, vol. 50, no. 2, pp. 528–537, 2012.
- [33] M. A. Veganzones, M. Simoes, G. Licciardi, N. Yokoya, J. M. Bioucas-Dias, and J. Chanussot, "Hyperspectral super-resolution of locally low rank images from complementary multisource data," *IEEE Transactions on Image Processing*, vol. 25, no. 1, pp. 274–288, 2016.
- [34] Q. Wei, J. Bioucas-Dias, N. Dobigeon, and J.-Y. Tourneret, "Hyperspectral and multispectral image fusion based on a sparse representation," *IEEE Transactions on Geoscience and Remote Sensing*, vol. 53, no. 7, 2015.
- [35] M. Simões, J. Bioucas-Dias, L. B. Almeida, and J. Chanussot, "A convex formulation for hyperspectral image superresolution via subspace-based regularization," *IEEE Transactions on Geoscience and Remote Sensing*, vol. 53, no. 6, pp. 3373–3388, 2015.
- [36] C. Dong, C. C. Loy, K. He, and X. Tang, "Image super-resolution using deep convolutional networks," *IEEE transactions on pattern analysis and machine intelligence*, vol. 38, no. 2, pp. 295–307, 2016.
- [37] J. Lu and D. Forsyth, "Sparse depth super resolution," *The IEEE Conference on Computer Vision and Pattern Recognition (CVPR)*, June 2015.
- [38] W. Shi, J. Caballero, F. Huszar, J. Totz, A. P. Aitken, R. Bishop, D. Rueckert, and Z. Wang, "Real-time single image and video super-resolution using an efficient sub-pixel convolutional neural network," *The IEEE Conference on Computer Vision and Pattern Recognition (CVPR)*, June 2016.
- [39] J. Kim, J. Kwon Lee, and K. Mu Lee, "Accurate image super-resolution using very deep convolutional networks," *The IEEE Conference on Computer Vision and Pattern Recognition (CVPR)*, June 2016.
- [40] —, "Deeply-recursive convolutional network for image super-resolution," *The IEEE Conference on Computer Vision and Pattern Recognition (CVPR)*, June 2016.
- [41] C. Ledig, L. Theis, F. Huszar, J. Caballero, A. Cunningham, A. Acosta, A. Aitken, A. Tejani, J. Totz, Z. Wang *et al.*, "Photo-realistic single image super-resolution using a generative adversarial network," *arXiv preprint arXiv:1609.04802*, 2016.
- [42] W.-S. Lai, J.-B. Huang, N. Ahuja, and M.-H. Yang, "Deep laplacian pyramid networks for fast and accurate super-resolution," *The IEEE Conference on Computer Vision and Pattern Recognition (CVPR)*, June 2017.
- [43] K. He, X. Zhang, S. Ren, and J. Sun, "Deep residual learning for image recognition," *The IEEE Conference on Computer Vision and Pattern Recognition (CVPR)*, pp. 770–778, 2016.
- [44] A. Bulat and G. Tzimiropoulos, "Super-fan: Integrated facial landmark localization and super-resolution of real-world low resolution faces in arbitrary poses with gans," *The IEEE Conference on Computer Vision and Pattern Recognition (CVPR)*, June 2018.
- [45] B. Haefner, Y. Quau, T. Mllenhoff, and D. Cremers, "Fight ill-posedness with ill-posedness: Single-shot variational depth super-resolution from shading," *The IEEE Conference on Computer Vision and Pattern Recognition (CVPR)*, June 2018.

- [46] X. Wang, K. Yu, C. Dong, and C. Change Loy, "Recovering realistic texture in image super-resolution by deep spatial feature transform," *The IEEE Conference on Computer Vision and Pattern Recognition (CVPR)*, June 2018.
- [47] Z. Hui, X. Wang, and X. Gao, "Fast and accurate single image super-resolution via information distillation network," *The IEEE Conference on Computer Vision and Pattern Recognition (CVPR)*, June 2018.
- [48] W. Han, S. Chang, D. Liu, M. Yu, M. Witbrock, and T. S. Huang, "Image super-resolution via dual-state recurrent networks," *The IEEE Conference on Computer Vision and Pattern Recognition (CVPR)*, June 2018.
- [49] M. Haris, G. Shakhnarovich, and N. Ukita, "Deep back-projection networks for super-resolution," *The IEEE Conference on Computer Vision and Pattern Recognition (CVPR)*, June 2018.
- [50] K. Zhang, W. Zuo, and L. Zhang, "Learning a single convolutional super-resolution network for multiple degradations," *The IEEE Conference on Computer Vision and Pattern Recognition (CVPR)*, June 2018.
- [51] Y. Chen, Y. Tai, X. Liu, C. Shen, and J. Yang, "Fsrnet: End-to-end learning face super-resolution with facial priors," *The IEEE Conference on Computer Vision and Pattern Recognition (CVPR)*, June 2018.
- [52] W. Huang, L. Xiao, Z. Wei, H. Liu, and S. Tang, "A new pan-sharpening method with deep neural networks," *IEEE Geoscience and Remote Sensing Letters*, vol. 12, no. 5, pp. 1037–1041, 2015.
- [53] G. Masi, D. Cozzolino, L. Verdoliva, and G. Scarpa, "Pansharpening by convolutional neural networks," *Remote Sensing*, vol. 8, no. 7, p. 594, 2016.
- [54] Y. Wei, Q. Yuan, H. Shen, and L. Zhang, "Boosting the accuracy of multi-spectral image pan-sharpening by learning a deep residual network," *arXiv preprint arXiv:1705.07556*, 2017.
- [55] J. M. Haut, R. Fernandez-Beltran, M. E. Paoletti, J. Plaza, A. Plaza, and F. Pla, "A new deep generative network for unsupervised remote sensing single-image super-resolution," *IEEE Transactions on Geoscience and Remote Sensing*, no. 99, pp. 1–19, 2018.
- [56] Y. Chang, L. Yan, H. Fang, S. Zhong, and W. Liao, "Hsi-denet: Hyperspectral image restoration via convolutional neural network," *IEEE Transactions on Geoscience and Remote Sensing*, no. 99, pp. 1–16, 2018.
- [57] C. Kwan, B. Budavari, A. C. Bovik, and G. Marchisio, "Blind quality assessment of fused worldview-3 images by using the combinations of pansharpening and hypersharpening paradigms," *IEEE Geoscience and Remote Sensing Letters*, vol. 14, no. 10, pp. 1835–1839, 2017.
- [58] C. Kwan, C. Haberle, A. Echavarren, B. Ayhan, B. Chou, B. Budavari, and S. Dickenshied, "Mars surface mineral abundance estimation using themis and tes images," *IEEE Ubiquitous Computing, Electronics and Mobile Communication Conference, New York City*, November 2018.
- [59] Y. Zhou, A. Rangarajan, and P. D. Gader, "Nonrigid registration of hyperspectral and color images with vastly different spatial and spectral resolutions for spectral unmixing and pansharpening," *2017 IEEE Conference on Computer Vision and Pattern Recognition Workshops (CVPRW)*, pp. 1571–1579, 2017.
- [60] F. D. Van der Meer, H. M. Van der Werff, F. J. Van Ruitenbeek, C. A. Hecker, W. H. Bakker, M. F. Noomen, M. Van Der Meijde, E. J. M. Carranza, J. B. De Smeth, and T. Woldai, "Multi-and hyperspectral geologic remote sensing: A review," *International Journal of Applied Earth Observation and Geoinformation*, vol. 14, no. 1, pp. 112–128, 2012.
- [61] Q. Wei, N. Dobigeon, and J.-Y. Tourneret, "Fast fusion of multi-band images based on solving a Sylvester equation," *IEEE Transactions on Image Processing*, vol. 24, no. 11, pp. 4109–4121, 2015.
- [62] H. Chui and A. Rangarajan, "A new point matching algorithm for non-rigid registration," *Computer Vision and Image Understanding*, vol. 89, no. 2-3, pp. 114–141, 2003.
- [63] X. Fan, H. Rhody, and E. Saber, "A spatial-feature-enhanced mmi algorithm for multimodal airborne image registration," *IEEE Transactions on Geoscience and Remote Sensing*, vol. 48, no. 6, pp. 2580–2589, 2010.
- [64] A. Myronenko and X. Song, "Point set registration: Coherent point drift," *IEEE transactions on pattern analysis and machine intelligence*, vol. 32, no. 12, pp. 2262–2275, 2010.
- [65] J. Ma, H. Zhou, J. Zhao, Y. Gao, J. Jiang, and J. Tian, "Robust feature matching for remote sensing image registration via locally linear transforming," *IEEE Transactions on Geoscience and Remote Sensing*, vol. 53, no. 12, pp. 6469–6481, 2015.
- [66] S. G. Mallat, "A theory for multiresolution signal decomposition: the wavelet representation," *IEEE Transactions on Pattern Analysis and Machine Intelligence*, vol. 11, no. 7, 1989.
- [67] M. J. Shensa, "The discrete wavelet transform: wedding the a trous and mallat algorithms," *IEEE Transactions on Signal Processing*, vol. 40, no. 10, pp. 2464–2482, 1992.
- [68] J. Liu, "Smoothing filter-based intensity modulation: A spectral preserve image fusion technique for improving spatial details," *International Journal of Remote Sensing*, vol. 21, no. 18, pp. 3461–3472, 2000.
- [69] P. Burt and E. Adelson, "The laplacian pyramid as a compact image code," *IEEE Transactions on Communications*, vol. 31, no. 4, pp. 532–540, 1983.
- [70] Q. Wei, N. Dobigeon, and J.-Y. Tourneret, "Bayesian fusion of hyper-spectral and multispectral images," *2014 IEEE International Conference on Acoustics, Speech and Signal Processing (ICASSP)*, 2014.
- [71] E. Wycoff, T.-H. Chan, K. Jia, W.-K. Ma, and Y. Ma, "A non-negative sparse promoting algorithm for high resolution hyperspectral imaging," *Acoustics, Speech and Signal Processing (ICASSP), 2013 IEEE International Conference on*, pp. 1409–1413, 2013.
- [72] C. Dong, C. C. Loy, K. He, and X. Tang, "Image super-resolution using deep convolutional networks," *arXiv preprint arXiv:1501.00092*, 2014.
- [73] K. Simonyan and A. Zisserman, "Very deep convolutional networks for large-scale image recognition," *arXiv preprint arXiv:1409.1556*, 2014.
- [74] J. Johnson, A. Alahi, and L. Fei-Fei, "Perceptual losses for real-time style transfer and super-resolution," *European Conference on Computer Vision*, pp. 694–711, 2016.
- [75] Y. Li, J. Hu, X. Zhao, W. Xie, and J. Li, "Hyperspectral image super-resolution using deep convolutional neural network," *Neurocomputing*, vol. 266, pp. 29–41, 2017.
- [76] R. Dian, S. Li, A. Guo, and L. Fang, "Deep hyperspectral image sharpening," *IEEE Transactions on Neural Networks and Learning Systems*, 2018.
- [77] J. Sethuraman, "A constructive definition of dirichlet priors," *Statistica sinica*, pp. 639–650, 1994.
- [78] E. Nalisnick and P. Smyth, "Deep generative models with stick-breaking priors," *ICML*, 2017.
- [79] P. Kumaraswamy, "A generalized probability density function for double-bounded random processes," *Journal of Hydrology*, vol. 46, no. 1-2, pp. 79–88, 1980.
- [80] C. Dugas, Y. Bengio, F. BÉlisle, C. Nadeau, and R. Garcia, "Incorporating second-order functional knowledge for better option pricing," *Advances in neural information processing systems*, pp. 472–478, 2001.
- [81] J. Han and C. Moraga, "The influence of the sigmoid function parameters on the speed of backpropagation learning," *From Natural to Artificial Neural Computation*, pp. 195–201, 1995.
- [82] G. Huang, Z. Liu, K. Q. Weinberger, and L. van der Maaten, "Densely connected convolutional networks," *arXiv preprint arXiv:1608.06993*, 2016.
- [83] J. B. Kinney and G. S. Atwal, "Equitability, mutual information, and the maximal information coefficient," *Proceedings of the National Academy of Sciences*, p. 201309933, 2014.
- [84] B. Zitova and J. Flusser, "Image registration methods: a survey," *Image and vision computing*, vol. 21, no. 11, pp. 977–1000, 2003.
- [85] J. Woo, M. Stone, and J. L. Prince, "Multimodal registration via mutual information incorporating geometric and spatial context," *IEEE Transactions on Image Processing*, vol. 24, no. 2, pp. 757–769, 2015.
- [86] I. Belghazi, S. Rajeswar, A. Baratin, R. D. Hjelm, and A. Courville, "Mine: mutual information neural estimation," *arXiv preprint arXiv:1801.04062*, 2018.
- [87] M. D. Donsker and S. S. Varadhan, "Asymptotic evaluation of certain markov process expectations for large time. iv," *Communications on Pure and Applied Mathematics*, vol. 36, no. 2, pp. 183–212, 1983.
- [88] R. D. Hjelm, A. Fedorov, S. Lavoie-Marchildon, K. Grewal, A. Trischler, and Y. Bengio, "Learning deep representations by mutual information estimation and maximization," *arXiv preprint arXiv:1808.06670*, 2018.
- [89] F. Nie, H. Huang, X. Cai, and C. H. Ding, "Efficient and robust feature selection via joint l_2, l_1 -norms minimization," pp. 1813–1821, 2010.
- [90] F. Yasuma, T. Mitsunaga, D. Iso, and S. K. Nayar, "Generalized assorted pixel camera: postcapture control of resolution, dynamic range, and spectrum," *IEEE Transactions on Image Processing*, vol. 19, no. 9, pp. 2241–2253, 2010.
- [91] L. Wald, T. Ranchin, and M. Mangolini, "Fusion of satellite images of different spatial resolutions: Assessing the quality of resulting images," *Photogrammetric Engineering & Remote Sensing*, vol. 63, no. 6, pp. 691–699, 1997.
- [92] F. A. Kruse, A. Lefkoff, J. Boardman, K. Heidebrecht, A. Shapiro, P. Barloon, and A. Goetz, "The spectral image processing system (sips) interactive visualization and analysis of imaging spectrometer data," *Remote sensing of environment*, vol. 44, no. 2-3, pp. 145–163, 1993.
- [93] N. Akhtar, F. Shafait, and A. Mian, "Hierarchical beta process with gaussian process prior for hyperspectral image super resolution," *European Conference on Computer Vision*, pp. 103–120, 2016.